

Article

Electromagnetic Design and End Effect Suppression of a Tubular Linear Voice Motor for Precision Vibrating Sieves

Meizhu Luo ¹, Zijiao Zhang ^{2,*}, Yan Jiang ² and Ji-an Duan ¹

¹ School of Mechanical and Electrical Engineering, Central South University, Changsha 410083, China; luomz2019@csu.edu.cn (M.L.)

² College of Electrical and Information Engineering, Hunan University, Changsha 410082, China

* Correspondence: zhangzijiao@hnu.edu.cn

Abstract: Precision vibrating sieves need a kind of power source, featuring small size, high frequency response, and small vibration amplitude. Linear Voice Coil Motor (LVCM) can achieve a high accelerated speed in a short stroke; it is an appropriate power source for the precision vibrating sieves. This paper designs a tubular LVCM with a volume no more than 6 cm³ and a stroke no less than 1.5 mm. The electromagnetic topology of this LVCM is established to validate its feasibility; the back Electromotive Force (back EMF) and the electromagnetic force are calculated. The end effect of this tubular LVCM is studied in detail; the auxiliary pole and the magnetic conductive stator base are designed to suppress its end detent force. Then, the main structure parameters are globally optimized by the multi-objective genetic algorithm to obtain better performance. The prototype of this tubular LVCM is manufactured and tested. The results of the experiments are compared with those of theoretical analyses. It is indicated that this tubular LVCM can provide an accelerated speed of 15g; g is the gravitational acceleration.

Keywords: linear voice coil motor (LVCM); high accelerated speed; end effect; electromagnetic design



Academic Editor: Hervé Morel

Received: 6 January 2025

Revised: 25 January 2025

Accepted: 1 February 2025

Published: 3 February 2025

Citation: Luo, M.; Zhang, Z.; Jiang, Y.; Duan, J.-a. Electromagnetic Design and End Effect Suppression of a Tubular Linear Voice Motor for Precision Vibrating Sieves. *Energies* **2025**, *18*, 704. <https://doi.org/10.3390/en18030704>

Copyright: © 2025 by the authors. Licensee MDPI, Basel, Switzerland. This article is an open access article distributed under the terms and conditions of the Creative Commons Attribution (CC BY) license (<https://creativecommons.org/licenses/by/4.0/>).

1. Introduction

Sorting systems for materials with tiny pieces need precision vibrating sieves with small, high-frequency vibrations. Small high-frequency vibrations require that their drive motors can provide high accelerated speeds in short strokes. In addition, these drive motors also should be small. Therefore, it is not applicable that the linear vibrations are achieved by the rotary motor and the movement conversion mechanism. The scheme of linear motor directly driving is ideal [1–4].

For linear motors, their accelerated speeds depend on the ratios of the thrusts to the mover masses. In those long stroke applications, Alternating Current (AC) linear motors have better performance at an accelerated speed, because they can produce higher electromagnetic thrusts [5–11]. However, for the short stroke applications, the requirements of high accelerated speeds and high speeds require the drive motors to have a small electrical time constant. It is clear that direct current (DC) motors have higher frequency responses than AC motors [2,12,13]. Thus, DC linear motors have advantages over AC linear motors in terms of the accelerated speed for the applications featuring small sizes and short strokes. Voice Coil Motor (VCM), as a kind of DC motor, features small size, light mover, high accelerated speed, and a quick response [14–16]. VCMs with high forces, low force ripples, and light movers are perfect for the micromotion units [17–19]. Thus, the

Linear Voice Coil Motor (LVCM) is preferred, considering the short stroke and the small size of the drive motor in the precision vibrating sieves.

The LVCM exhibited in this paper is a moving coil type to reduce the volume and the mass of its mover. Its stator is composed of three ring permanent magnets, the fillers, the iron yoke, the auxiliary pole, and the stator base. The ring permanent magnets and their filler are hollow circular cylinder shapes, and the magnetization direction of three ring permanent magnets is the longitudinal direction of this LVCM, aiming at reducing the motor size and the number of permanent magnets.

The paper is organized as follows: Section 2 studies the electromagnetic topology of the tubular LVCM to verify its feasibility; the key structure parameters for back Electromotive Force (back EMF) and the electromagnetic force are pointed out; Section 3 analyzes the suppression of the end effect by the method of adding the auxiliary poles and optimizing the stator base thickness, which is simple and effective; the optimization of its main structure parameters is described in Section 4, aiming at high accelerated speed and small volume; the prototype and the experimental analysis of this tubular LVCM are provided in Section 5.

2. Electromagnetic Topology of Tubular LVCM

This tubular LVCM has three ring permanent magnets and three ring DC coils, as exhibited in Figure 1. The mover of the tubular VCM includes the three coils and the coil supporter. The coil supporter is made of a lightweight aluminum alloy; it is a kind of un-conducted magnetic material.

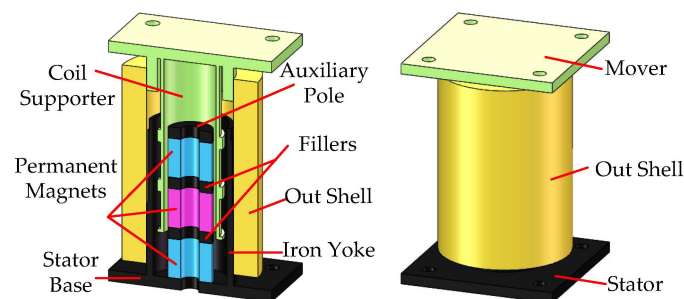


Figure 1. Structure of the tubular LVCM.

Three permanent magnets are magnetized in the longitudinal direction and set in the motor stator. The electromagnetic structure of this stator mainly includes two parts, which can be noted as the inner part and the outer part. The inner part of the motor stator has three permanent magnets, two fillers, and the auxiliary pole. The outer part of the motor stator is only an iron yoke. The stator base connects the inner part and the outer part. The auxiliary pole on the top of the inner part and the fillers between the permanent magnets are made of a magnetic conductive material. The magnetic field lines have access to the air gap and the coils through the two fillers and the auxiliary pole. The outer part, which is an iron yoke, can help the magnetic field lines close and reduce the reluctance of the main magnetic circuit. There is no iron yoke inside the inner part; that is, the inner part is a hollow structure.

The reluctance of the magnetic circuit inside the inner part of the motor stator is larger, and the magnetic fluxes prefer to take the paths with low reluctances; thus, the major magnetic flux crosses through the gap between the inner part and the outer part. The motor mover runs in the gap. The effective electromagnetic force, which is a Lorentz force, can be generated when the major magnetic flux passes the energized coils. There is a stator base at the bottom of the stator; it is also made of the magnetic conductive material. The designs of the auxiliary pole and the magnetic conductive stator base can help to suppress the end detent force of this LVCM.

The accelerated speed of this LVCM should be higher than 150 m/s^2 (which is about $15g$; g is the gravitational acceleration); an average thrust of 2.4 N can meet the need if the mover mass is lower than 16 g . As a result, the coils are designed to be very thin to reduce the mover mass and reluctance of the main magnetic circuit. In addition, the stroke of this LVCM is only 1.5 mm , so the volume and the mass of the motor mover are very small. That is beneficial to the high accelerated speed.

Back EMF and the electromagnetic force are the most important electromagnetic parameters in a novel motor; they will be calculated below.

2.1. Back Electromotive Force

This tubular LVCM is a symmetric cylinder. The radial directions (r) of the circular faces in this cylinder are the directions of the effective magnetic flux in the gap. The axial direction (x) of this cylinder is the running direction of the motor mover. The cross-section of x - r is taken to calculate the back EMF, as shown in Figure 2. In Figure 2, the three coils are noted as ①, ②, and ③ the two fillers are noted as ④ and ⑤.

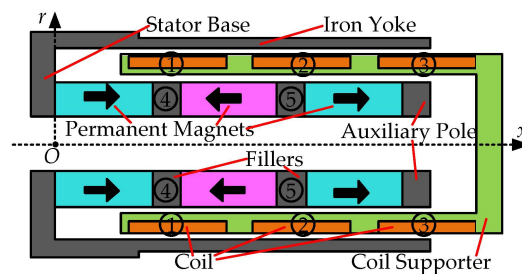


Figure 2. Cross-section of x - r in the tubular LVCM.

As Figure 2 shows, the three permanent magnets are magnetized in the longitudinal direction (x); the magnetic flux lines straightly pass the gap (where the coils are set in) through Filler ④, Filler ⑤, and the auxiliary pole. The stroke of this LVCM is only 1.5 mm , so Filler ④ is always pointed at Coil ①, Filler ⑤ is always pointed at Coil ②, and the auxiliary pole is always pointed at Coil ③ during this tubular LVCM running. The direct currents in Coil ① and Coil ③ have the same direction; the direct current in Coil ② is reversed. The running direction of the motor mover will change when the direct current directions of Coil ①/③ and Coil ② are interchanged. This tubular VCM is an axially symmetrical structure, so the analytical model (exhibited in Figure 3) only takes half of the cross-section x - r , which is shown in Figure 2.

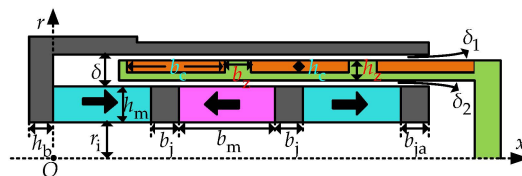


Figure 3. Analytical model for the tubular LVCM.

In Figure 3, h_m is the radial thickness of three permanent magnets and b_m is their axial length; the two fillers and the auxiliary pole have the same radial thickness as three permanent magnets, the axial length of two fillers is b_j , the axial length of the auxiliary pole is b_{ja} , the radius of the hollow structure inside the inner part is r_i , and the axial thickness of the stator base is h_b . h_c is the radial thickness of three coils, and b_c is their axial length. h_z and b_z are the radial thickness and the axial length of the parts of the coil supporter between coils, respectively. δ is the radial length of the air gap between the inner part and the outer part of the mover stator, δ_1 is the radial length of the mechanical air gap

between the motor mover and the outer part of the motor stator, and δ_2 is the radial length of the mechanical air gap between the motor mover and the inner part of the motor stator. According to this analytical model, the distribution $B_m(x, r)$ of the magnetic flux in the gap of this tubular LVCM is calculated, $B_{mr}(x, r)$ is its radial component, and $B_{ma}(x, r)$ is its axial component.

$$B_{mr}(x, r) = \sum_{n=1,3,5\dots}^{\infty} \frac{n\pi}{b_j + b_m} M_{0n} \left[e^{\frac{n\pi(r+2r_i+2h_m+2\delta)}{b_j+b_m}} + e^{-\frac{n\pi(r+2r_i+2h_m)}{b_j+b_m}} \right] \cdot \cos \frac{n\pi x}{b_j + b_m} \quad (1)$$

$$B_{ma}(x, r) = \sum_{n=1,3,5\dots}^{\infty} \frac{n\pi}{b_j + b_m} M_{0n} \left[e^{\frac{n\pi(r+2r_i+2h_m+2\delta)}{b_j+b_m}} - e^{-\frac{n\pi(r+2r_i+2h_m)}{b_j+b_m}} \right] \cdot \sin \frac{n\pi x}{b_j + b_m} \quad (2)$$

where n is the harmonic order and $M_{0n} = \frac{4B_r(b_j+b_m)}{n^2\pi^2} \cdot \sin \frac{n\pi b_j}{2(b_j+b_m)} \cdot \frac{1-e^{-\frac{2n\pi(r_i+h_m)}{b_j+b_m}}}{2-2e^{-\frac{2n\pi(r_i+h_m+\delta)}{b_j+b_m}}}$. The curves exhibited in Figure 4 are $B_{mr}(x, r)$ and $B_{ma}(x, r)$ when r is taken as the value of the middle line in the coils.

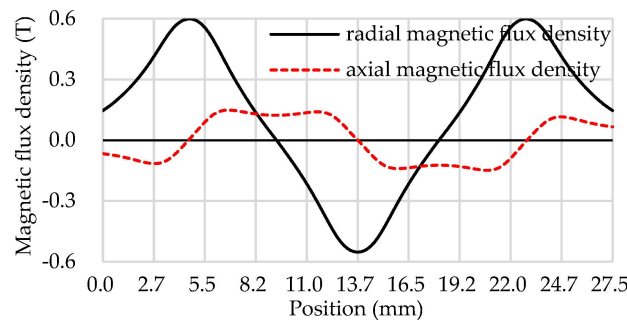


Figure 4. Distribution of the magnetic flux in the gap of this tubular LVCM.

The conductors in three coils cut the magnetic flux lines as this LVCM runs, and then the back EMF is generated. The permeability of the permanent magnet is set as μ , B_r is the residual magnetic flux density of the permanent magnet, and $lc(r)$ is the circumference of the conductors in the radial positions of r ($lc(r) = 2\pi r$). $B_{mr}(x, r)$ is the radial component of $B_m(x, r)$, so it is the one generating the back EMF $E(t)$,

$$E(t) = \int_{r_i+h_m+\delta_2+h_z-h_c}^{r_i+h_m+\delta_2+h_z} \left[\int_{B_m-vt}^{b_c+b_m-vt} B_{mr}(x, r)lc(r)v dx - \int_{2b_m-vt}^{b_c+2b_m-vt} B_{mr}(x, r)lc(r)v dx + \int_{3b_m-vt}^{b_c+3b_m-vt} B_{mr}(x, r)lc(r)v dx \right] dr \quad (3)$$

when, $C_{0n} = \frac{4B_r v}{n} \cdot \sin \frac{n\pi b_j}{2(b_j+b_m)} \cdot \left(r_i + h_m + \delta_2 + h_z - \frac{h_c}{2} \right)$ and $C_{1n} = \frac{e^{-\frac{2n\pi h_m}{b_j+b_m}} - 1}{1 - e^{-\frac{2n\pi(\delta+h_m)}{b_j+b_m}}}$, the

back EMF $E(t)$ can be deduced as

$$E(t) = \sum_{n=1,3,5\dots}^{\infty} C_{0n} \cdot C_{1n} \cdot \left[e^{\frac{n\pi(r_i+h_m+\delta_2+h_z)}{b_j+b_m}} - e^{\frac{n\pi(r_i+h_m+\delta_2+h_z-h_c)}{b_j+b_m}} \right] \cdot \sin \frac{n\pi vt}{b_j + b_m} \quad (4)$$

where, $-(b_c - b_j)/2 \leq t \leq (b_c - b_j)/2$. The curve drawn by Formula (4) is exhibited as the calculation result in Figure 5, and the other curve is the back EMF obtained by the simulation when the motor mover runs 1.5 mm.

This tubular LVCM is a DC motor, thus, the back EMF is a DC motor. In the simulation, the power supplied for the LVCM is produced by a virtual switching voltage source to be closer to the situation of this tubular LVCM actually working. Therefore, the simulation result obtains noticeable noise, which come from the power provided by the virtual switching voltage source. However, the curve tendency and the average value of the calculation

result can well match the simulation result in Figure 5. The amplitude and the variation of the back EMF can meet the requirements; the feasibility of this tubular LVCM is verified.

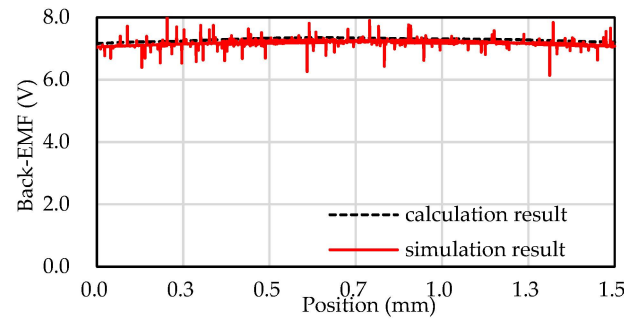


Figure 5. Curves of back EMF.

2.2. Electromagnetic Force

DC currents flow into the three coils during this tubular LVCM running, and the major magnetic flux, which is excited by the permanent magnets, passes the energized coils, so a Lorentz force (it is the electromagnetic force F of this tubular LVCM) is generated. The magnetic flux density is different when the mover is in a different position. The position of the motor mover is noted as x_m . Thus, $F(x_m)$ can be given by

$$F(x_m) = \int_{r_i+h_m+\delta_2+h_z-h_c}^{r_i+h_m+\delta_2+h_z} \frac{I \cdot N \cdot l_c(r)}{b_c \cdot h_c} \left[\int_{x_m}^{x_m+b_c} B_{mr}(x, r) dx - \int_{x_m+b_c+b_z}^{x_m+2b_c+b_z} B_{mr}(x, r) dx + \int_{x_m+2b_c+2b_z}^{x_m+3b_c+2b_z} B_{mr}(x, r) dx \right] dr \quad (5)$$

where, I is the current passing through each conductor in the three coils and N is the number of the conductors in each coil. When, $C_{2n} = \frac{4INB_r}{nb_ch_c} \cdot \sin \frac{n\pi b_j}{2(b_j+b_m)} \cdot \left(r_i + h_m + \delta_2 + h_z - \frac{h_c}{2} \right)$, $F(x_m)$ should be

$$F(x_m) = \sum_{n=1,3,5\dots}^{\infty} C_{2n} \cdot C_{1n} \cdot \left[e^{\frac{n\pi(r_i+h_m+\delta_2+h_z)}{b_j+b_m}} - e^{\frac{n\pi(r_i+h_m+\delta_2+h_z-h_c)}{b_j+b_m}} \right] \cdot \sin \frac{n\pi x_m}{b_j + b_m} \quad (6)$$

The curve drawn by Formula (6) and the curve of the electromagnetic force obtained by the simulation are both shown in Figure 6 when the motor mover runs 1.5 mm.

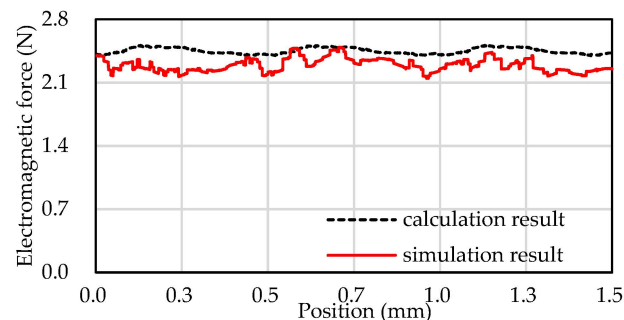


Figure 6. Curves of electromagnetic force F —mover position x_m .

The simulation result has some noise compared to the calculation result; this is for the same reason in the analysis of back EMF. In addition, the curve achieved by analytical calculation can well match the one achieved by the simulation; the amplitude and the ripple of the electromagnetic force are both satisfying. In addition, it can be seen that the parameters that have the most influence on back EMF and the electromagnetic force are h_m , b_m , b_j , b_{ja} , r_i , δ_1 , δ_2 , h_z , h_c , and b_c . These parameters should be optimized by the multi-objective genetic algorithm.

3. End Effect Suppression of Tubular LVCM

The end effect suppression can help to reduce the thrust ripple of this tubular LVCM, and it is beneficial to improve the accelerated speed (F/m , m is the mass of the motor mover). This tubular LVCM adopts the method of adding the auxiliary poles and the magnetic conductive stator base to suppress its end effect, which is simple and effective. The distribution of the magnetic flow in the analytical model (exhibited in Figure 3) is shown in Figure 7.

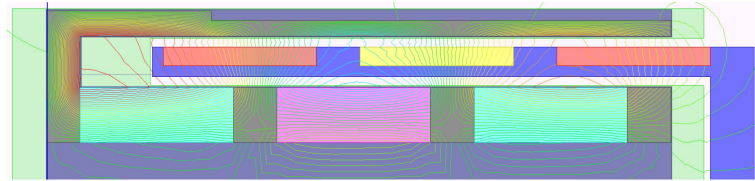


Figure 7. Distribution of the magnetic flow in this tubular LVCM.

The end effects of linear motors are caused by the longitudinal breaking of their electromagnetic structures. For the distribution of the magnetic flow in Figure 7, it can be seen that the auxiliary poles and the magnetic conductive stator base of this tubular LVCM can provide an easier closed path for the magnetic flow. So, the end effect of this tubular LVCM is suppressed; the key parameters in this section are the axial length b_{ja} of the auxiliary pole and the axial thickness h_b of the stator base.

The distribution function of the longitudinal magnetic flux density under the ideal conditions is periodic. However, the function will turn into a step one because of the electromagnetic structure breaking. A step factor $f_p(x)$ can be introduced to solve this problem.

$$f_p(x) = \begin{cases} 0 & x < 0 \\ 1 & 0 \leq x \leq 3b_m + 2b_j \\ 0 & x > 3b_m + 2b_j \end{cases} \tag{7}$$

In addition, two compensation factors, $f_{ef1}(x)$ and $f_{ef2}(x)$, are added because of the auxiliary poles and the magnetic conductive stator base.

$$f_{ef1}(x) = \begin{cases} 0 & x < -h_b \\ 1 & -h_b \leq x \leq 0 \\ 0 & x > 0 \end{cases} \tag{8}$$

$$f_{ef2}(x) = \begin{cases} 0 & x < 3b_m + 2b_j \\ 1 & 3b_m + 2b_j \leq x \leq 3b_m + 2b_j + b_{ja} \\ 0 & x > 3b_m + 2b_j + b_{ja} \end{cases} \tag{9}$$

Then the magnetization intensity $M_{ef}(x)$ under the impacts of the end effect and its suppression design can be calculated by the magnetization intensity $M(x)$ obtained by the initial ideal model.

$$M_{ef}(x) = M(x) \cdot (f_p(x) + M_{1n}f_{ef1}(x) + M_{2n}f_{ef2}(x)) \tag{10}$$

where, $M(x) = \sum_{n=1,3,5,\dots}^{\infty} \frac{4B_r}{n\pi\mu} \cdot \sin\frac{n\pi b_j}{2(b_j+b_m)} \cdot \cos\frac{n\pi x_m}{b_j+b_m}$, $M_{1n} = \frac{e^{\frac{2n\pi h_b}{b_j+b_m}} - 1}{2n\pi(h_b+h_m+\delta)}$, $M_{2n} = \frac{e^{-\frac{2n\pi b_{ja}}{b_j+b_m}} - 1}{2n\pi(b_{ja}+h_m+\delta)}$. The magnetic flux $B_{mef}(x, r)$ in the gap of this tubular LVCM, under the impacts of the end effect and its suppression design, is derived by the magnetization inten-

sity $M_{ef}(x)$. The electromagnetic force $F(x_m)$ exhibited in Formula (6) is also recalculated by $B_{mef}(x, r)$ instead of $B_{mr}(x, r)$. When F_{ave} is the average value of the electromagnetic force $F(x_m)$, the thrust ripple ratio of this tubular LVCM is its thrust ripple divided by $2 F_{ave}$. For linear motors, the end effect can be directly reflected in the thrust ripple ratio. Figure 8 shows the changes of the thrust ripple ratio under various combinations of b_{ja} and h_b .

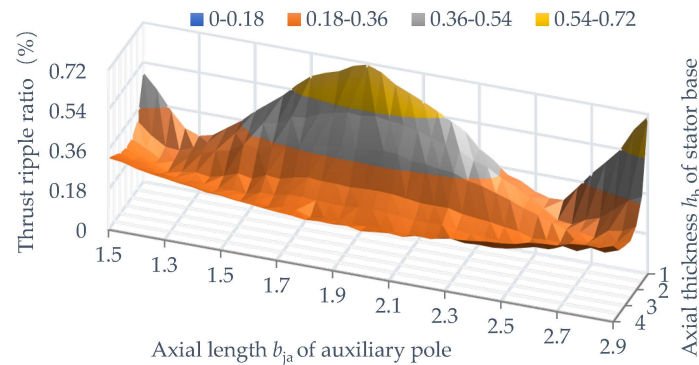


Figure 8. Thrust ripple ratio—the axial length b_{ja} of the auxiliary pole/the axial thickness h_b of the stator base.

For the data in Figure 8, the thrust ripple ratio can be reduced by increasing the axial thickness h_b of the stator base as a whole, but the reducing effect will be insignificant when h_b is larger than 3.5 mm. The impact on the thrust ripple ratio caused by the axial length b_{ja} of the auxiliary pole is stronger than the one caused by h_b . In addition, there are two states of the thrust ripple ratio changes caused by b_{ja} : when h_b is smaller than 3.5 mm, the thrust ripple ratio changes have two low-valley regions, which are near $b_{ja} = 1.4$ mm or 2.6 mm, respectively; when h_b is larger than 3.5 mm, the thrust ripple ratio changes have one low-valley region, which is near $b_{ja} = 1.8$ mm. So, it can be deduced that the axial thickness h_b of the stator base influences the end effect of this tubular LVCM by acting on the magnetic saturation, meaning it is sufficient as long as h_b is larger than a certain number (3.5 mm in this motor). The impact of b_{ja} on the end effect has a certain periodicity; the thrust ripple ratio is well reduced when the impact of b_{ja} on the end effect matches with the periodic distribution of the magnetic field. Considering the motor size, the mover mass, and the thrust characteristics, the value of b_{ja} should be selected within the first low-valley region (which is the one near $h_b = 1.4$ mm in Figure 8).

During the calculation of the thrust ripple ratio here, it is found that the key parameters (h_b and b_{ja}) for the end effect of this tubular LVCM also act on the average value of the electromagnetic force. In addition, the average electromagnetic force strongly relates to the parameters ($h_m, b_m, b_j, r_i, \delta_1, \delta_2, h_z, h_c,$ and b_c), which is obtained in Section 2. Thus, the multi-objective genetic algorithm will be adopted to optimize parameters that have coupling relationships with each other.

4. Parameter Optimization of Tubular LVCM

The tubular LVCM is designed for the precision vibrating sieves; its accelerated speed (which is the force/mass ratio) should be as high as possible, and the volume of this motor should be as small as possible. There are many parameters of this tubular LVCM that have influences on the motor performances, and these parameters also affect each other. So, the main structure parameters are globally optimized by the multi-objective genetic algorithm [20–22] to obtain better performances in this section.

The goals of this optimization are the high accelerated speed (F/m , m is the mass of the motor mover) and the small volume (V_m) of this tubular LVCM. During the optimization, the Latin hypercubic sampling method with constraints is adopted to obtain the initial

samples of the proxy model for the prediction accuracy. The calculations (including back EMF, the electromagnetic force, and the end effect) achieved in Sections 2 and 3 provide the electromagnetic performances of the different scenarios. Basic data for the globally multi-objective optimization are obtained by the finite element analysis.

First, the impacts of the main parameters (according to the analyses in Sections 2 and 3, the main parameters are h_m , b_m , b_j , r_i , δ_1 , δ_2 , h_z , h_c , b_c , h_b , and b_{ja}) on the performances of this tubular LVCM are calculated by the finite element method and provided to the multi-objective genetic algorithm optimization. The analytical ranges of these parameters can be obtained, as listed in Table 1.

Table 1. Analytical ranges of the optimization variables.

Optimization Variable	Structure Parameter	Initial Value	Analytical Range
V1	Radial thickness of three permanent magnets h_m	2.50 mm	2.00~3.00 mm
V2	Axial length of three permanent magnets b_m	7.00 mm	6.00~8.00 mm
V3	Axial length of two fillers b_j	2.00 mm	1.50~2.50 mm
V4	Radius of the hollow structure inside the inner part r_i	2.00 mm	1.50~3.00 mm
V5	Radial length of the air gap between the inner part and the outer part of the mover stator δ_1	0.50 mm	0.30~0.70 mm
V6	Radial length of the mechanical air gap between the motor mover and the inner part of the motor stator δ_2	0.50 mm	0.30~0.70 mm
V7	Radial thickness of the parts of the coil supporter between coils h_z	1.35 mm	1.20~1.50 mm
V8	Radial thickness of three coils h_c	0.85 mm	0.70~1.00 mm
V9	Axial length of three coils b_c	7.00 mm	6.00~8.00 mm
V10	the axial thickness of the stator base h_b	3.50 mm	3.00~5.00 mm
V11	Axial length of the auxiliary pole b_{ja}	2.50 mm	1.50~3.50 mm

According to the analytical ranges of the optimization parameters given in Table 1, the objective function for the optimization targets is proposed as follows:

$$\left[\max\left(\frac{F}{m}\right), \min(F_{pk-pk}), \min(V_m) \right] \quad (11)$$

where F_{pk-pk} is the peak-to-peak value of the electromagnetic force F , also is the thrust ripple of this tubular LVCM. F_{pk-pk} is strongly related to the end effect. Q_1 , Q_2 , and Q_3 are weight coefficients of F/m , F_{pk-pk} , and V_m , respectively. In addition, Q_1 , Q_2 , and Q_3 are set as 0.5, 0.3, and 0.2.

For the parametric sensitivity analyses of the optimization targets (the accelerated speed F/m , the thrust ripple F_{pk-pk} , and the motor volume V_m), $2n - 1$ different bias variance terms ($D_i, D_{ij}, \dots, D_{1,2,\dots,n}$) compose the output variance (D) of the corresponding results, so the sum of the $2n - 1$ variance terms ($D_i, D_{ij}, \dots, D_{1,2,\dots,n}$) is D . The sensitivity coefficients ($S_i, S_{ij}, \dots, S_{1,2,\dots,n}$) of parameters are obtained by $2n - 1$ different bias variance terms ($D_i, D_{ij}, \dots, D_{1,2,\dots,n}$) dividing the output variance (D), that is,

$$1 = \sum_{i=1}^n S_i + \sum_{1 \leq i < j \leq n} S_{ij} + \dots + S_{1,2,\dots,n} \quad (12)$$

S_i is the first-order sensitivity, which means the influence of one individual optimization variable on the objective function. $S_{ij}, \dots, S_{1,2,\dots,n}$ are the second-order sensitivity to the n th-order sensitivity, which means the coupling influences of multiple optimization variables on the objective function. The total sensitivity coefficient S_i^T of one individual optimization variable can be obtained by the calculations of all its sensitivities with different orders,

$$S_i^T = S_i + \sum_{i \neq j}^n S_{ij} + \dots + S_{1,2,\dots,n} \quad (13)$$

The sampling analyses of the eleven optimization variables are completed, combined with the finite element calculations, and the total sensitivity coefficients of the eleven optimization variables for the three motor performances (motor volume, average electromagnetic force, thrust ripple ratio) are shown in Figure 9.

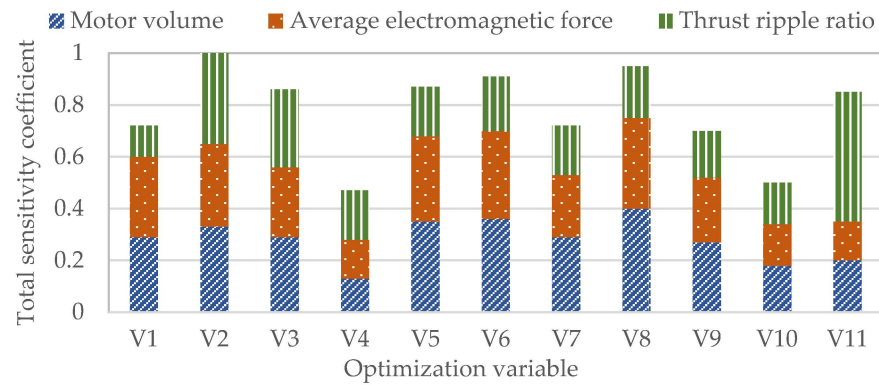


Figure 9. Total sensitivity coefficients—optimization variables.

After the global optimization with the multi-objective genetic algorithm, three motor performances (motor volume, average electromagnetic force, and thrust ripple ratio) are improved by 7.53%, 8.67%, and 10.6%, respectively.

5. Prototype and Experiment

Based on the globally optimized results, the prototype of the tubular LVCM is processed, as exhibited in Figure 10. The volume of this prototype is 5.5 cm³ (which is only 91.67% of the original design value of 6 cm³), its stroke is 1.6 mm, which is longer than the original design value of 1.5 mm, and the mass of the motor mover is only 16 g. So the prototype realizes the goal of a smaller motor volume as well as the demand of the mover stroke.

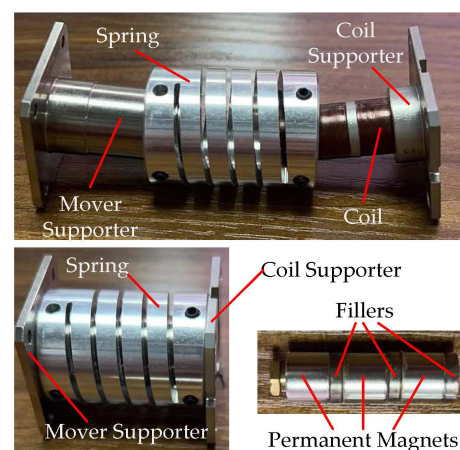


Figure 10. Prototype of this tubular LVCM.

Back EMF and the force characteristics of this prototype are tested, and the data are compared with the theoretical analyses (including the calculation result and the simulation result). Figure 11 shows the experiment result of back EMF.

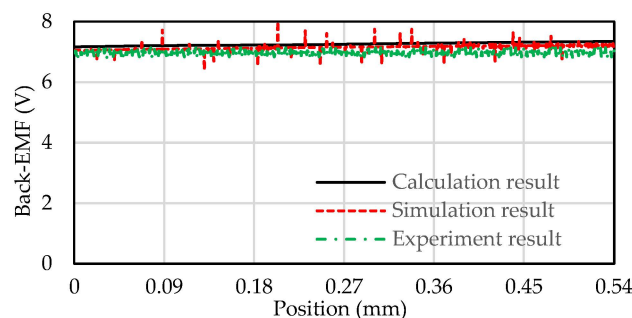


Figure 11. Back EMF of the prototype.

The average value of the experiment result of back EMF is 6.94 V; the ones of its calculation result and simulation result are 7.26 V and 7.15 V, respectively. The error of the experiment result to the calculation result is 4.41%, and the error of the experiment result to the simulation result is 2.94%, both of the errors are lower than 5%, which is the engineering allowable value. Figure 12 is the comparison of the calculation result, the simulation result, and the experiment result for the electromagnetic force.

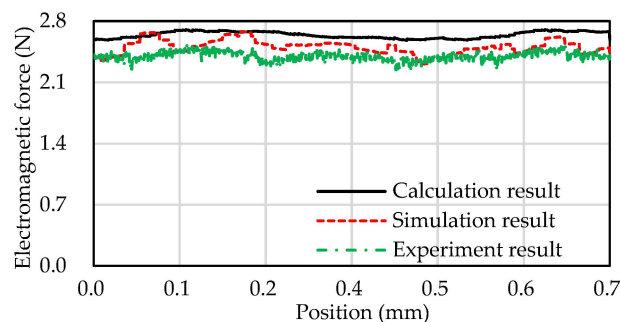


Figure 12. Thrust of the prototype.

The average values of the calculation result, the simulation result, and the experiment result in Figure 12 are 2.64 N, 2.50 N, and 2.41 N, respectively. The error of the experiment result to the simulation result on the average electromagnetic force is 3.60%, which is acceptable. The thrust ripple ratio of the calculation result, the simulation result, and the experiment result in Figure 12 are 3.53%, 2.87%, and 3.01%, respectively. The simulation result of the thrust ripple ratio is obtained by the global optimization, so it is much better than the calculation result. In addition, the experiment result of the thrust ripple ratio is higher than the simulation one by 4.87%, due to the machining error and the inconsistency of material properties. However, it still is lower than 5%, and the test accelerated speed is 150.63 m/s^2 , which can meet the demand.

Thus, the feasibility of the motor can be verified.

6. Conclusions

This paper provides the design and analysis of a tubular LVCM. The electromagnetic topology of this LVCM is studied, including back EMF and the electromagnetic force. The auxiliary pole and the magnetic conductive stator base are designed to suppress the end effect. In addition, the main structure parameters are globally optimized by the multi-objective genetic algorithm. Based on the analysis, a prototype is manufactured; experimental data indicate the analysis results. The following are some of the inferences from the analysis and experiment results:

(1) The key structure parameters (h_m , b_m , b_j , b_{ja} , r_i , δ_1 , δ_2 , h_z , h_c , and b_c) acting on back EMF and the electromagnetic force are obtained through their derivations. These parameters should be adopted in the global optimization.

(2) The impact on the thrust ripple ratio caused by the axial length b_{ja} of the auxiliary pole is stronger than the one caused by h_b . h_b should be larger than 3.5 mm, and the impact of b_{ja} on the end effect has a certain periodicity. b_{ja} and h_b also are the key parameters for the global optimization.

(3) The motor volume, the average electromagnetic force, and the thrust ripple ratio are improved by 7.53%, 8.67%, and 10.6%, respectively, through the global optimization with the multi-objective genetic algorithm.

(4) After the experiment test of this prototype, the average value of the experiment result of back EMF is 6.94 V, the average value of the electromagnetic force is 2.41 N, the thrust ripple ratio is 3.01%, the test accelerated speed is 150.63 m/s², the motor volume is 5.5 cm³ (which is only 91.67% of the original design value 6 cm³), and its stroke is 1.6 mm, which is longer than the original design value 1.5 mm. The characteristics are satisfactory and can meet the demands.

Author Contributions: M.L. contributed to this research article in the formal analysis, investigation, resources, data curation, and writing of the original draft. Z.Z. contributed to this research article for conceptualization and methodology. Y.J. and J.-a.D. contributed to this research article for writing expression. All authors have read and agreed to the published version of the manuscript.

Funding: This research was funded by the National Natural Science Foundation of China under Grant 52377048 and the Natural Science Foundation of Hunan Province of China under Grant 2023JJ30159.

Data Availability Statement: The original contributions presented in this study are included in the article. Further inquiries can be directed to the corresponding author(s).

Conflicts of Interest: The authors declare no conflicts of interest.

References

1. Yi, Z.; Luo, M.; Duan, J.-a.; Jiang, Y. Adaptive feedforward control based on estimated electromagnetic parameters upon a novel two-degrees-of-freedom actuator with a unibody magnetic circuit. *Energies* **2024**, *17*, 3017. [[CrossRef](#)]
2. Xing, F.Z.; Kwon, B.I. Design of a rotary-linear motor with unipolar SPM and voice coil structure. *IEEE Access* **2020**, *8*, 150291–150300. [[CrossRef](#)]
3. Sun, Q.; Wang, M.; Liu, M.; Zhang, C.; Li, L. Magnetic field distortion analysis and suppression for the minimum unit winding segmented moving-magnet linear motor. *IEEE Trans. Ind. Electron.* **2024**, *71*, 3452–3460. [[CrossRef](#)]
4. Li, P.; Liu, C.; Wang, B.; Li, C.; Zhan, R.; Peng, J.; Cheng, Z.; Jiang, L. The investigation of strategy to suppress thrust fluctuations in electromagnetic halbach coreless linear motor. *IEEE Trans. Appl. Supercond.* **2024**, *34*, 3603804. [[CrossRef](#)]
5. Du, C.; Zhang, L.; Niu, X.; Yang, K. Characteristics analysis and comparison of a cylindrical linear induction motor with composite secondary structure. *Energies* **2024**, *17*, 1294. [[CrossRef](#)]
6. Yu, C.; Ma, J.; Pan, H.; Basin, M.V. Adaptive iterative learning constrained control for linear-motor-driven gantry stage. *IEEE/ASME Trans. Mechatron.* **2024**, *29*, 1647–1658. [[CrossRef](#)]
7. Cui, L.; Lv, G.; Liu, Y.; Zhi, R. Steady-state analysis and modeling of a special modular transverse flux linear synchronous Motor. *IEEE Trans. Energy Convers.* **2023**, *38*, 2938–2946. [[CrossRef](#)]
8. Zhang, Z.; Luo, M.; Duan, J.-A.; Kou, B. Design and analysis of a novel frequency modulation secondary for high-speed permanent magnet linear synchronous motor. *IEEE/ASME Trans. Mechatron.* **2022**, *27*, 790–799. [[CrossRef](#)]
9. Wen, T.; Xiang, B.; Wang, Z.; Zhang, S. Speed control of segmented PMLSM based on improved SMC and speed compensation model. *Energies* **2020**, *13*, 981. [[CrossRef](#)]
10. Cui, F.; Sun, Z.; Xu, W.; Qian, H.; Cao, C. Optimization analysis of long primary permanent magnet linear synchronous motor. *IEEE Trans. Appl. Supercond.* **2021**, *31*, 0603504. [[CrossRef](#)]
11. Zhou, W.; Sun, Z.; Cui, F.; Mao, Y. Electromagnetic design of high-speed and high-thrust cross-shaped linear induction motor. *IEEE Access* **2021**, *9*, 87501–87509. [[CrossRef](#)]
12. Xu, G.Y.; Zheng, J.X. Analysis of electromagnetic characteristics of novel tubular permanent magnet brushless DC linear motor for medical equipment. *Mechatron. Syst. Control.* **2024**, *52*, 25–31. [[CrossRef](#)]

13. Zhang, Y.; Gono, R.; Jasinski, M. An improvement in dynamic behavior of single phase PM brushless DC motor using deep neural network and mixture of experts. *IEEE Access* **2023**, *11*, 64260–64271. [[CrossRef](#)]
14. Mu, J.; Zhang, H.; Lou, Y.; Zhao, Y.; Kou, B. Design and analysis of a double layer coils linear motor with series magnetic circuit structure using for linear dynamic loading platform. In Proceedings of the 2023 IEEE International Magnetic Conference, Sendai, Japan, 15–19 May 2023.
15. Zhang, H.; Kou, B.; Ge, Q.; Liu, Y. Design and analysis of a high thrust linear voice coil motor using for the stiffness test of linear motor servo system. *IEEE Trans. Magn.* **2022**, *58*, 8200505. [[CrossRef](#)]
16. Shewale, M.S.; Razban, A.; Deshmukh, S.P.; Mulik, S.; Zambare, H.B. Design and experimental validation of voice coil motor for high precision applications. In Proceedings of the 2021 13th International Symposium on Linear Drives for Industry Applications, Wuhan, China, 1–3 July 2021.
17. Kim, J.Y.; Ahn, D. Analysis of high force voice coil motors for magnetic levitation. *Actuators* **2021**, *9*, 133. [[CrossRef](#)]
18. Yu, B.; Ren, W.; Wang, Y.; Wang, L. A novel structure for minimization of thrust ripple on voice coil motor used in ventilators. In Proceedings of the 2021 13th International Symposium on Linear Drives for Industry Applications, Wuhan, China, 1–3 July 2021.
19. Zhang, Z.; Luo, M.; Zhou, H.; Duan, J.-A. Design and analysis of a novel two-degree-of-freedom voice coil motor. *IEEE/ASME Trans. Mechatron.* **2019**, *24*, 2908–2918. [[CrossRef](#)]
20. Zhu, S.; Li, X.; Hu, J.; Jiang, R.; Liu, C.; Wang, K. Multi-objective optimization of permanent magnet assisted synchronous reluctance motor for industrial drive using three-step optimization method. *IEEE Trans. Appl. Supercond.* **2024**, *61*, 218–230. [[CrossRef](#)]
21. Guo, J.; Su, J. Study of multiobjective genetic algorithm on Taylor external fixation. *IEEE Access* **2022**, *10*, 46986–46999. [[CrossRef](#)]
22. Avsar, Y.; Fenercioglu, A.; Soyaslan, M. Design optimization of PM synchronous motor: Rail mounted belt drive elevator systems. *IEEE Trans. Ind. Appl.* **2024**, *60*, 301–311. [[CrossRef](#)]

Disclaimer/Publisher’s Note: The statements, opinions and data contained in all publications are solely those of the individual author(s) and contributor(s) and not of MDPI and/or the editor(s). MDPI and/or the editor(s) disclaim responsibility for any injury to people or property resulting from any ideas, methods, instructions or products referred to in the content.